International Journal of Heat and Mass Transfer 152 (2020) 119481

Contents lists available at ScienceDirect

International Journal of Heat and Mass Transfer

journal homepage: www.elsevier.com/locate/hmt

Strong electron-phonon coupling induced anomalous phonon transport in ultrahigh temperature ceramics ZrB_2 and TiB_2

Jia-Yue Yang[a,b,*], Wenjie Zhang[a,b], Chengying Xu[c], Jun Liu[c], Linhua Liu[a,b], Ming Hu[d,*]

[a] School of Energy and Power Engineering, Shandong University, Jinan, Shandong 250061, China
[b] Optics & Thermal Radiation Research Center, Shandong University, Qingdao, Shandong 266237, China
[c] Department of Mechanical and Aerospace Engineering, North Carolina State University, Raleigh, NC 27695, USA
[d] Department of Mechanical Engineering, University of South Carolina, Columbia, SC 29208, USA

ARTICLE INFO

Article history:
Received 6 October 2019
Revised 20 January 2020
Accepted 5 February 2020

Keywords:
Thermal transport
Phonon
Electron-phonon interaction
Grain boundary scattering

ABSTRACT

Ultrahigh temperature ZrB_2- and TiB_2-based ceramics are widely used in extreme thermal environment. Yet, open questions remain pertaining to their lattice thermal conductivity (κ_{ph}). In this work we investigate the phonon transport of ZrB_2 and TiB_2 by systematically evaluating the phonon-phonon interaction (PPI), electron-phonon interaction (EPI) and grain boundary scattering (GBS) from the atomistic level using first-principles. Upon including EPI, the room-temperature κ_{ph} of ZrB_2 and TiB_2 is significantly reduced by 38.16% and 52.34%, respectively, and agrees excellently with experimental measurement. Such giant reduction arises from the strong EPI for the heat-carrying acoustic phonons due to phonon anomaly and the existence of Fermi nesting vectors along high symmetry line in the Brillouin zone. Following the Casimir model, the GBS further decreases κ_{ph} of ZrB_2 even by 49.27% for small grain boundary spacing of 50 nm and theoretical calculations agree well with experiments. Thus, GBS crucially influences phonon transport, which explains the large deviation of previous experimental measurements on κ_{ph} for ZrB_2-based ceramics. Moreover, the combined influence of EPI and GBS results in the anomalous phonon transport where κ_{ph} is almost temperature-independent over a large temperature range, consistent with experimental observations. This work directly reveals the phonon transport mechanism for high temperature ceramics ZrB_2 and TiB_2, gains deep insight into the large variation in the previously reported κ_{ph} and provides guidance to engineer it for practical applications.

1. Introduction

Ultrahigh temperature ceramics, which are mainly based on transition metal borides, nitrides, and carbides, are a class of refractory ceramics with high melting temperatures and excellent chemical stability [1–3]. Among them, transition metal borides such as ZrB_2 and HfB_2 outstand by their extremely high melting temperatures (>3000 °C), low density, and chemical inertness against molten metals [3]. As such, they are excellent candidate materials for applications involving extremely high temperature environments [4–6], including hypersonic vehicles [5], reentry spacecraft [7], propulsion systems, and refractory crucibles [3]. Also, these materials demonstrate high thermal and electrical conductivity, which promotes them as potential buffer materials for microelectronics [8,9]. Therefore, fully exploiting thermal transport in ultrahigh temperature ceramics is of great importance to advance them in those above applications.

In transition metal borides, the total high thermal conductivity (κ_{tot}) is intrinsically separated into the electron (κ_{el}) and phonon contributions (κ_{ph}) [10]. Following the Wiedemann-Franz law [11], the electron part κ_{el} can be obtained from the measured electrical conductivity σ by $\kappa_{el} = L\sigma T$, where L is the Lorentz number (2.45×10^{-8} WΩ/K^2) and T is the absolute temperature. In contrast, the phononic component κ_{ph} cannot be measured directly. One can estimate κ_{ph} by subtracting κ_{el} from the measured κ_{tot}. This is the practical route to separate the electronic and phononic contribution to the total thermal transport. Yet, the above estimated κ_{ph} may be prone to error and may result in opposite conclusion owing to different techniques and quality of samples used in experiments. Taking ZrB_2 for instance, Thompson et al. [12] showed that κ_{ph} was less than approximately 12 W/mK at room temperature and concluded that electrons were the dominant thermal carriers. However, Zimmermann et al. [13] found that κ_{ph} was as high as 24 W/mK below 200 °C. Zhang and co-workers [14] even obtained

* Corresponding authors.
E-mail addresses: jy_yang@sdu.edu.cn (J.-Y. Yang), hu@sc.edu (M. Hu).

https://doi.org/10.1016/j.ijheatmasstransfer.2020.119481
0017-9310/

negative κ_{ph} for their produced ZrB_2 samples. Thus, there are still open questions regarding κ_{ph} of transition metal diborides by indirectly estimating from the experimentally measured κ_{tot} using the Wiedemann-Franz law, which requires a more accurate way to directly evaluate it.

Accurately accessing κ_{ph} of transition metal diborides can not only resolve the above open questions, but also be crucial to provide physical insights into the phonon transport mechanisms of the ultrahigh temperature ceramics. Based on the empirical Green-Kubo equilibrium molecular dynamics (GK-EMD) simulations, Lawson et al. [15] directly evaluated κ_{ph} of ZrB_2 and HfB_2. The theoretically predicted κ_{ph} agreed excellently with experiments [16] at room temperature but began to deviate largely at higher temperatures, e.g., when temperature increases to 1000 K. The accuracy of the empirical atomistic simulations depends crucially on the developed Tersoff style interatomic potentials, which usually only calibrate thermodynamic properties of target materials near room temperature, and suffers from transferability at high temperatures. Unlike GK-EMD, first-principles method based on the anharmonic lattice dynamics (ALD) directly studies the anharmonic interactions among phonons and can accurately access κ_{ph} without empirical parameters [17–21]. In metal transition compounds, the phonon contribution to thermal transport involves a temperature-dependent competition between anharmonic phonon-phonon and electron-phonon interactions. Using first-principles simulations, Li et al. [22] showed that κ_{ph} decreases rapidly with increasing temperature for typical metallic and nonmetallic crystals, but becomes nearly temperature-independent for the group-V transition metal carbides. In those compounds, there exist nested Fermi surfaces and large frequency gaps between acoustic and optic phonons, resulting in the much stronger electron-phonon interaction than its phonon-phonon counterpart. This study identifies an anomalous heat flow regime driven by the interplay between phonon dispersions and Fermi nesting surface.

In this work, we present the phonon transport behaviors of transition metal borides ZrB_2 and TiB_2 using first-principles calculations, and observe an anomaly in the temperature-dependent κ_{ph}. The combination of strong electron-phonon interaction (EPI) and grain boundary scattering (GBS) leads to the almost temperature-independent κ_{ph}, which agrees excellently with previous experimental observations. In contrast to previous first-principles study of group-V transition metal carbides, our present study highlights the significant role of EPI and GBS in hindering the phonon transport in the transition metal borides, which provides a new phonon transport mechanism.

2. Methods

For phonon transport process, the quasiparticle phonons are scattered by other phonons, isotopes, electrons, and grain boundaries. At thermal equilibrium, the lattice thermal conductivity κ_{ph} can be expressed as [20]

$$\kappa_{ph}^{\alpha\beta} = \sum_{\mathbf{q}\nu} C_{\mathbf{q}\nu} \upsilon_{\mathbf{q}\nu}^{\alpha} \upsilon_{\mathbf{q}\nu}^{\beta} \tau_{\mathbf{q}\nu}, \tag{1}$$

where $C_{\boldsymbol{q}\nu}$, $\upsilon_{\boldsymbol{q}\nu}$ and $\tau_{\boldsymbol{q}\nu}$ is the specific heat capacity, group velocity and relaxation lifetime for a phonon in the ν branch at $\boldsymbol{q}$ point, respectively. Following the Matthiessen's rule [23], we calculate the total phonon scattering rate by $1/\tau_{\mathbf{q}\nu} = 1/\tau_{\mathbf{q}\nu}^{ph-ph} + 1/\tau_{\mathbf{q}\nu}^{iso} + 1/\tau_{\mathbf{q}\nu}^{el-ph} + 1/\tau^{b}$, which is contributed by scattering from other phonons, isotopes, electrons, and grain boundaries, respectively. Intrinsically, the phonon-phonon interaction (PPI) involves in the creation or annihilation of new phonons. Within the lowest-order three-phonon scattering process, $1/\tau_{\mathbf{q}\nu}^{ph-ph}$ can be determined from the anharmonic third-order interatomic force constants (IFCs). The phonon-isotope scattering originates from the mass disorder and can be estimated from first-principles. In this work, the phonon-isotope scattering is automatically included into PPI and not exclusively studied. The EPI normally occurs when phonons participate in the electronic interband or intraband transition. Consequently, phonons are absorbed or emitted. Based on the density functional perturbation theory (DFPT), the self-energy of phonon mode $\boldsymbol{q}\nu$ read [24,25]

$$\Pi_{\mathbf{q}\nu}(\omega, T) = 2\sum_{mn} \int \frac{d\mathbf{k}}{\Omega} |g_{mn,\nu}(\mathbf{k}, \mathbf{q})|^{2} \frac{f_{n\mathbf{k}}(T) - f_{m\mathbf{k}+\mathbf{q}}(T)}{\omega + \varepsilon_F - \varepsilon_{m\mathbf{k}+\mathbf{q}} - \omega + i\delta_0}. \tag{2}$$

The $g_{mn,\nu}$ ($\mathbf{k}$, $\mathbf{q}$) matrix quantifies the electron-phonon scattering process between energy state n$\mathbf{k}$ and m$\mathbf{k}$+$\boldsymbol{q}$, and can be evaluated at arbitrary large $\mathbf{k}$ and $\mathbf{q}$ mesh using the Wannier code. The $f_{n\mathbf{k}}$ stands for the Fermi-Dirac distribution and ε_F is the Fermi energy, respectively. The factor 2 takes into account spin degeneracy and small value δ_0 is introduced to guarantee numerical stability. The electron-phonon scattering rate is given by $1/\tau_{\mathbf{q}\nu}^{EPI} = 2\mathrm{Im}(\Pi_{\mathbf{q}\nu})/\hbar$. In the spark plasma-sintered ZrB_2-based polycrystalline ceramics, GBS is shown to substantially influence thermal transport of single crystals. [15] Therefore, it is necessary to quantify the contribution of GBS to κ_{ph}. Within the Casimir limit [26], the grain boundary scattering rate is given by $1/\tau^{b} = \upsilon_g/L$, where υ_g is the phonon group velocity and L is the grain boundary spacing. In the Casimir model, the GBS is approximated as phonon frequency independent and its strength is a constant and unaffected by the grain boundary characteristics except the GB spacing L. Previous studies [13] have reported values on grain size in ZrB_2-based polycrystalline ceramics. Yet, there were no data on L and no clear relation between L and grain size, so in this work we gradually change the value of L and reveal how different grain boundary spacing reduces the lattice thermal conductivity.

To calculate κ_{ph} from first-principles, details about phonon frequency, velocity and specific heat capacity are also required, which can be extracted from the harmonic IFCs. To obtain the harmonic and third-order anharmonic IFCs, a large $5 \times 5 \times 5$ supercell containing 375 atoms was built and the fifth nearest neighbor shell was chosen. Those first-principles calculations were performed with the Quantum Espresso [27] package using the Optimized Normal-Conserving Vanderbilt pseudopotentials (ONCVPSP) within the local density approximation (LDA) [28]. After obtaining the above IFCs, the contribution of phonon-phonon and phonon-isotope scattering to κ_{ph} was evaluated with the ShengBTE package [29]. The $\tau_{\mathbf{q}\nu}^{EPI}$ was computed with the EPW program [24,25] (details see Supplementary Material) which is based on the DFPT and maximally localized Wannier functions to obtain phonon linewidth arising from EPI. By performing the electron-phonon scattering calculations, the coarse k- and q-mesh was initially chosen as $12 \times 12 \times 12$ and $6 \times 6 \times 6$, and then Wannier interpolated to a much denser mesh of $25 \times 25 \times 25$ and $15 \times 15 \times 15$, respectively (more computational details see Supplementary Material). With the collected phonon relaxation time, the individual contribution of PPI, EPI, and GBS to κ_{ph} can be quantified.

3. Results and discussions

Thermophysical properties of solids such as specific heat capacity and heat conduction depend on their phonon dispersion behaviors. Thus, it is important to firstly analyze the lattice dynamics of phonons prior to studying their transport properties. Fig. 1 presents the phonon dispersion curve of ZrB_2 and TiB_2 along the high-symmetry lines in the first Brillouin zone with the correction of linewidth induced by the electron-phonon coupling at 300 K. A relatively large frequency gap of approximately 5 THz is observed between acoustic and optic phonons for ZrB_2, due to

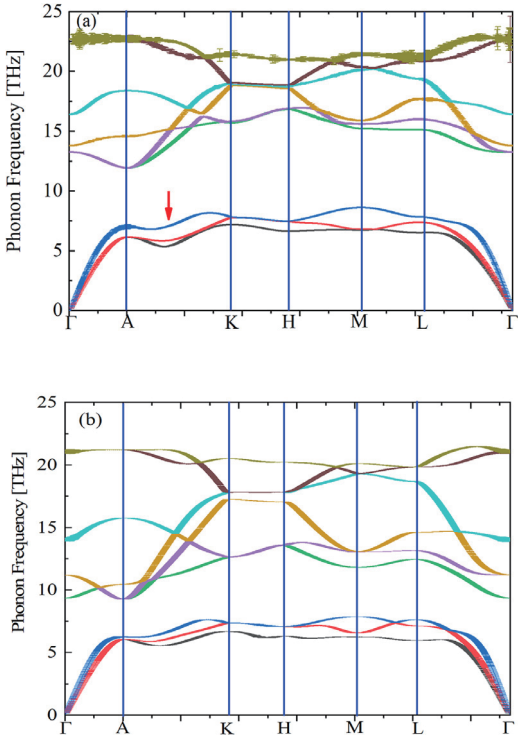

Fig. 1. The theoretically calculated phonon dispersion curve along the high-symmetry lines for (a) ZrB_2 and (b) TiB_2 with the correction of linewidth induced by the electron-phonon coupling at 300 K. The red arrow points out the phonon softening along the A (0 0 1/2) → K (1/3 1/3 0) line. (For interpretation of the references to color in this figure legend, the reader is referred to the web version of this article.)

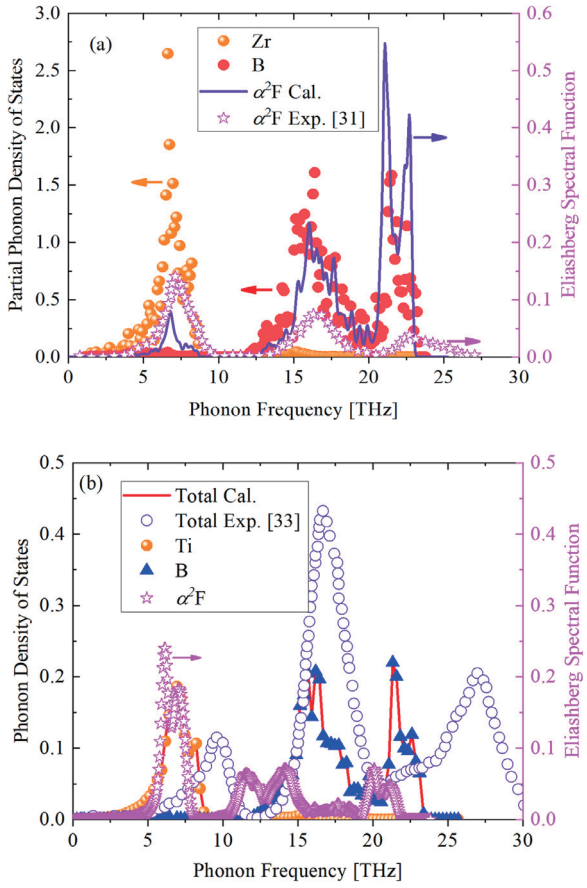

Fig. 2. The calculated total and partial phonon density of states and Eliashberg spectral function (α^2F) of (a) ZrB_2 and (b) TiB_2, in comparison with literature experiment [31,33].

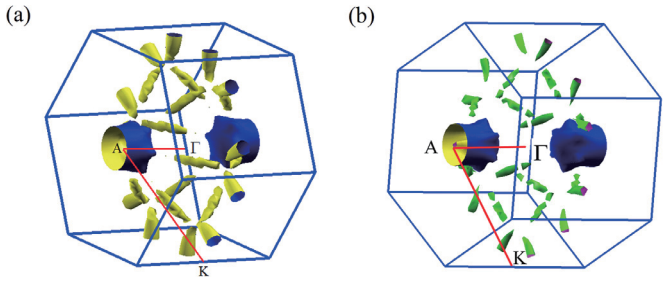

Fig. 3. The calculated Fermi surface of (a) ZrB_2 and (b) TiB_2. Images are prepared using XCrysden [39]. Ring-like electron surface and wrinkled dumbbell-like hole sheet observed around the K (1/3 1/3 0) and A (0 0 1/2) symmetry point, respectively.

the large mass difference between Zr atoms (91.22 amu) and B atoms (10.81 amu). Yet, for TiB_2, the frequency gap is reduced to approximately 2.5 THz due to the relatively light Ti atoms (47.87 amu). Note that heat is carried primarily by the low-lying acoustic phonons in these materials, and thermal resistance is intrinsically caused by the scattering between (i) an acoustic phonon and two optic phonons (*aoo*), (ii) two acoustic phonons and an optic phonon (*aao*), or (iii) three acoustic phonons (*aaa*). The presence of large frequency gap in ZrB_2 normally prohibits *aao* scattering process. Considering that the bandwidth of high-lying acoustic phonons is relatively narrow, it will restrict the *aao* scattering process to the low frequency regions where the *aaa* process is much stronger [30]. Therefore, *aaa* process is the primary scattering that limits κ_{ph}.

The large frequency gap will decouple the vibrations of transition metal Zr and B. In Fig. 2(a), it illustrates that the vibrations of Zr atom mainly contribute to the acoustic phonons lying between 0 and 8 THz, and the B atom with lower mass vibrates at higher frequency above 12 THz. The large amount of atom vibrations tends to perturb interatomic potentials and results in the strong EPI. Based on the DFPT calculations, the Eliashberg spectral function (α^2F) which quantifies the electron-phonon coupling strength is presented and demonstrates a good agreement with experiment [31], as shown in Fig. 2(a). Though the averaged electron-phonon coupling strength λ is quite low with the value of 0.17, in good agreement with 0.15 of literature data [32], we observe three strong peaks located at approximately 7 THz, 17 THz, and 22 THz, respectively. The locations of those major peaks agree excellently with that of phonon density of states contributed by Zr and B atoms, indicating that strong EPI arises from local atomic vibrations. Similar phenomenon is also observed in TiB_2. In Fig. 2(b), the Ti atom vibrations contributes primarily to the low part (0–8 THz) of the calculated total phonon density of state which agrees overall with the inelastic neutron scattering experiments [33]. Yet, there exists discrepancy in the peak positions and amplitude, which is plausibly caused by the fact that the chosen "frozen phonon" method fails due to the presence of the strong electron-phonon coupling. The averaged electron-phonon coupling strength λ is 0.16, in good agreement with 0.15 of literature data [32]. Compared with ZrB_2, the dominant peak of α^2F is located around the heat-carrying acoustic phonons in TiB_2. Previous studies [22,34–36] showed that Fermi nesting surface tended to induce strong interaction between electrons and phonons. To explain the strong EPI, we compute the Fermi surfaces of ZrB_2 and TiB_2 in the Brillouin zone. In Fig. 3, theoretical calculations show a wrinkled dumbbell-like hole sheet and a ring-like electron sheet

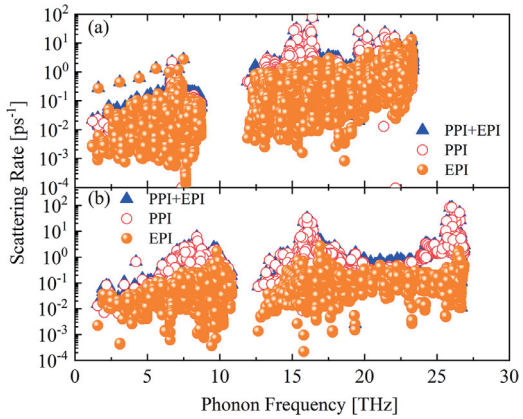

Fig. 4. The frequency-dependent phonon scattering rate individually contributed by PPI and EPI in (a) ZrB_2 and (b) TiB_2.

around the symmetry A (0 0 1/2) and K (1/3 1/3 0) point in ZrB_2 and TiB_2, which are consistent with the Fermi surface calculated by Tanaka [37] and Sichkar et al. [32] With the ring-like electron and wrinkled dumbbell-like hole sheets, nesting vectors along the high symmetry Γ-A-K directions are observed. In ZrB_2, with the partially filled *d*-electron band, its short-range correlation nature increases the electronic polarizability in a resonance-like manner [35], giving rise to strong EPI. The strong interplay between electrons and phonons tends to renormalize phonon energies and produces phonon anomalies. In Fig. 1, a phonon softening along the A-K line is observed in the phonon dispersions of ZrB_2. In TiB_2, a sharp rod locates at the center of the wrinkled dumbbell-like hole around A point, which indicates the potential strong interplay between electrons and phonons.

For the low-lying acoustic phonons, the strong EPI will modify self-energy and induce large linewidth of acoustic phonons, as shown in Fig. 1. Since the *aaa* process primarily contributes to the intrinsic thermal resistance, the inclusion of strong EPI certainly affects the phonon transport properties. By decomposing the total phonon scattering rate into the individual contribution from the PPI and EPI, it observes that EPI overwhelms PPI especially for the high-lying acoustic phonons of ZrB_2 and TiB_2, as shown in Fig. 4. For ZrB_2, a strong EPI influence on the scattering rate for the heat-carrying phonons between 5–8 THz is observed. While for TiB_2, the strong EPI effect is observed near the edge of acoustic phonon bands.

After collecting phonon scattering rate, the lattice thermal conductivity κ_{ph} can be evaluated. In Fig. 5, the calculated temperature-dependent κ_{ph} of ZrB_2 and TiB_2 contributed individually by PPI, EPI and GBS is presented, in comparison with literature experimental and theoretical data [13,15,16]. Here, the phonon-isotope scattering is included into the PPI and not separately treated. With its hexagonal lattice, ZrB_2 demonstrates a slight anisotropy in κ_{ph}, where $\kappa_{ph}^{\perp}$ and $\kappa_{ph}^{\parallel}$ corresponds to lattice thermal conductivity perpendicular and parallel to the *c*-axis, respectively. However, the experimental data in literature did not explicitly consider such anisotropy [12–14], so we choose the average with the form of $(\kappa_{ph}^{\perp}+2\kappa_{ph}^{\parallel})/3$ for ZrB_2 and TiB_2 in this work. For the pure ZrB_2 and TiB_2 crystal, the intrinsic thermal resistance arises from PPI and EPI. Only considering PPI, the calculated κ_{ph} of ZrB_2 at room temperature is 79.15 W/mK. Upon including EPI, κ_{ph} is reduced to 49 W/mK (by 38.16%) and demonstrates good agreement with the measured 51 W/mK [37] and coincidently matches the calculated 54 W/mK [15] using classical GK-EMD. The agreement with experimental result of ZrB_2 suggests that EPI is crucial to accurately determine κ_{ph}. For the spark plasma-sintered

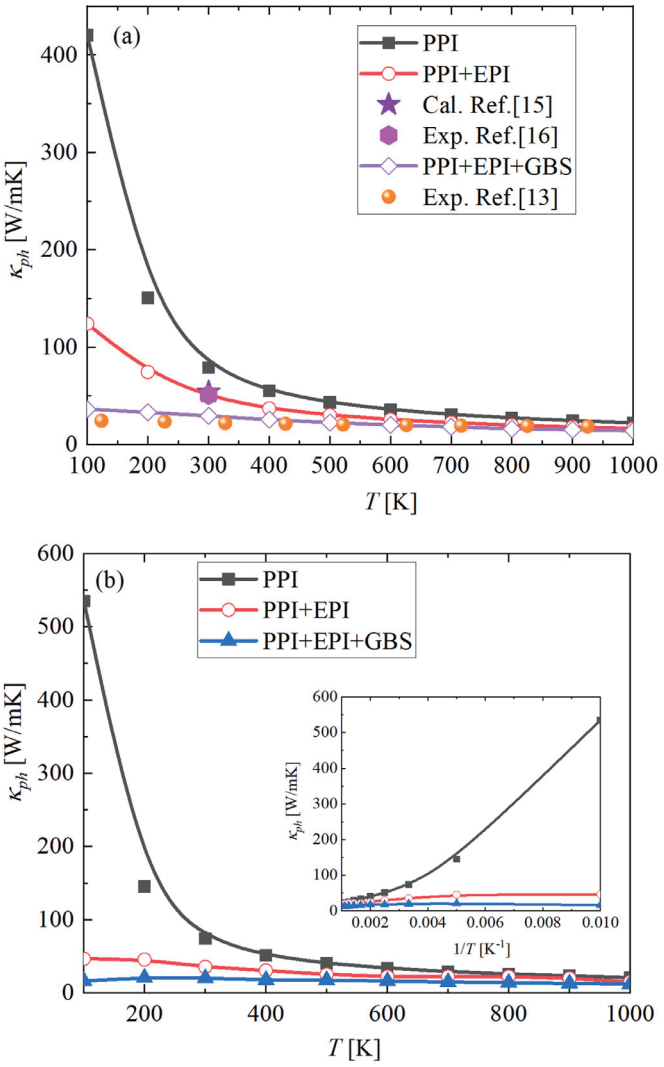

Fig. 5. The calculated temperature-dependent κ_{ph} of (a) ZrB_2 and (b) TiB_2 including phonon-phonon interaction (PPI), electron-phonon interaction (EPI), and grain boundary scattering (GBS), compared with the available literature data [13,15,16]. The grain boundary spacing is chosen as 100 nm both for ZrB_2 and TiB_2. The inset presents the κ_{ph} vs $1/T$ for TiB_2.

ZrB_2-based polycrystalline ceramics, κ_{ph} is as low as approximately 20 W/mK at 300 K and GBS is primarily responsible for such large reduction. Following the Casimir model $1/\tau^b = v_g/L$, where the highest v_g for acoustic phonon is calculated to 5.36 km/s and the GB spacing L is approximated as 100 nm, the room-temperature κ_{ph} is further reduced to 29 W/mK (by 25.32%) upon the inclusion of GBS, consistent with the measured 24 W/mK [13]. Furthermore, by further reducing L by half to 50 nm, the κ_{ph} will significantly reduce to approximately 10 W/mK (by 49.27%), which agrees well with the estimated 12 W/mK [12]. Considering that the grain size for the ZrB_2-based ceramics was reported as approximately 13 μm in Ref. [13], almost twice as large as that in Ref. [12], and the larger grain size introduces larger L. The theoretical predictions are consistent with the changing trend of κ_{ph} with decreasing grain size in experimental observations. Thus, we can conclude that the GBS plays a critical role in reducing κ_{ph} of ZrB_2-based polycrystalline ceramics and determining its variation with increasing temperature. Considering that previous studies may synthesize samples with various grain sizes, it is reasonable to explain why different studies reported κ_{ph} of ZrB_2-based polycrystalline ceramics with such a large difference. It also shows that κ_{ph} exhibits anomalous

temperature-independence by combining the effect of EPI and GBS, in good agreement with experimental observation. By only considering PPI and EPI, κ_{ph} gradually decreases with increasing temperature, as shown in Fig. 5(a). This can be understood in terms of the fact that at higher temperatures the electron-phonon coupling becomes strong and further decreases phonon lifetime. While the GBS is temperature-independent, the combination of EPI and GBS leads to the temperature-independence, which indicates that GBS plays the significant role in the anomalous behavior of κ_{ph}.

For TiB_2, an anomalous phonon transport is observed upon including EPI, as shown in Fig. 5(b). At 300 K, the very strong EPI effect reduces the κ_{ph} of TiB_2 from 73.82 W/mK to 35.26 W/mK (by 52.34%). Moreover, the κ_{ph} of TiB_2 is nearly temperature independent and deviates from the typical behavior of $\kappa_{ph} \sim 1/T$. The weak temperature dependence of the lattice thermal conductivity of TiB_2 is in line with the same strong electron-phonon coupling in VN, as evidenced in recent experimental study [38]. In the insert of Fig. 5(b), it observes that κ_{ph} is almost linear with $1/T$ only considering the intrinsic PPI. Yet, upon including EPI, it shows that κ_{ph} is almost a constant and changes slightly with $1/T$. By further including GBS, the value of κ_{ph} is reduced slightly but its anomalous temperature-independence remains. Such anomalous phonon transport is also observed in the group V transition metal carbides such as NbC and it is assumed to be primarily caused by the strong interactions between electrons and phonons due to the existence of Fermi nesting vectors [22]. By further analyzing the Fermi surface and strong EPI effect on phonon scattering, we show that the anomalous phonon transport in TiB_2 is mainly caused by the existence of wrinkled dumbbell-like hole sheets and sharp rod. Moreover, in comparison with ZrB_2, the EPI effect on the phonon transport of TiB_2 is much stronger. That is because the anomalous phonon transport is caused by the metallic *d*-electron band [35], and when going from TiB_2 to ZrB_2, the *d*-electron band gets partially filled, which slightly reduces the strong interplay between electrons and phonons.

4. Conclusions

In summary, we directly evaluate the phonon transport of ultrahigh temperature ZrB_2 and TiB_2 ceramics using first-principles and quantify the individual contribution of phonon-phonon scattering, electron-phonon coupling and grain boundary scattering. Within the three-phonon scattering scheme, the room-temperature κ_{ph} of ZrB_2 and TiB_2 is predicted as 79.15 W/mK and 73.82 W/mK and largely reduced to 49 W/mK and 35.26 W/mK (by 38.16% and 52.34%), respectively, upon the inclusion of electron-phonon coupling, which agrees excellently with experiment. The large reduction of κ_{ph} is mainly caused by the strong EPI for the heat-carrying acoustic phonons which is contributed by the transition metal atom vibrations. The strong interactions between electrons and phonons arise from the nested Fermi vectors along the high symmetry Γ-A-K directions in the Brillouin zone. Furthermore, the grain boundary scattering effect is included following the Casimir model. The lattice thermal conductivity can be significantly reduced to 10 W/mK by 49.27% with a very small grain boundary spacing of 50 nm. Those theoretical simulations are consistent with previous experiments, which suggests that grain boundary scattering is the dominant reason to explain the large difference in the reported κ_{ph}. Moreover, by combining the electron-phonon interaction and grain boundary scattering, the anomalous phonon transport phenomenon is observed, where κ_{ph} has little change with temperature. Our studies provide a deep insight into the role of electron-phonon coupling and grain boundary scattering in of ZrB_2 and TiB_2 and the understanding gained from this work is expected to help manipulate thermal conductivity of ultrahigh temperature ceramics.

Declaration of Competing Interest

The authors declare that they have no known competing financial interests or personal relationships that could have appeared to influence the work reported in this paper.

CRediT authorship contribution statement

Jia-Yue Yang: Writing - original draft. **Wenjie Zhang:** Formal analysis. **Chengying Xu:** Formal analysis. **Jun Liu:** Formal analysis, Writing - review & editing. **Linhua Liu:** Formal analysis, Writing - review & editing. **Ming Hu:** Writing - review & editing.

Acknowledgments

J.-Y. Y. is grateful for the support from Shandong University (Qilu Young Scholar 89963031) and gratefully acknowledges the computing time granted by the supercomputing system in the Supercomputing Center, Shandong University, Weihai. C.Y X. and J. L. acknowledge the support by the Faculty Research and Professional Development Fund by North Carolina State University. L. L. acknowledges the support by the National Natural Science Foundation of China (Grant no. 51336002). Research reported in this publication was supported in part by the NSF (award number 1905775) and SC EPSCoR/IDeA Program under NSF OIA-1655740 via SC EPSCoR/IDeA 20-SA05 and GEAR-CRP2019 19-GC02. The views, perspective, and content do not necessarily represent the official views of the SC EPSCoR/IDeA Program nor those of the NSF.

Supplementary materials

Supplementary material associated with this article can be found, in the online version, at doi:10.1016/j.ijheatmasstransfer.2020.119481.

References

[1] M.J. Gasch, D.T. Ellerby, S.M. Johnson, Ultra high temperature ceramic composites, in: N.P. Bansal (Ed.), Handbook of Ceramic Composites, Kluwer Academic, Boston, 2005, p. 197.
[2] K. Upadhya, J. Yang, W. Hoffman, Am. Ceram. Soc. Bull. 76 (12) (1997) 51.
[3] W.G. Fahrenholtz, G.E. Hilmas, I.G. Talmy, J.A. Zaykoski, J. Am. Ceram. Soc. 90 (5) (2007) 1347.
[4] G.J. Harrington, G.E. Hilmas, Thermal conductivity of ZrB_2 and HfB_2, in: W.G. Fahrenholtz, E.J. Wuchina, W.E. Lee, Y. Zhou (Eds.), Ultra-High Temperature Ceramics: Materials for Extreme Environment Applications, John Wiley & Sons, Inc., 2014, p. 197.
[5] D. Van Wie, D. Drewry, D. King, C. Hudson, J. Mater. Sci. 39 (19) (2004) 5915–5924.
[6] E. Wuchina, E. Opila, M. Opeka, W. Fahrenholtz, I. Talmy, Electrochem. Soc. Inter. 16 (4) (2007) 30.
[7] A.S. Brown, Aerosp. Am. 35 (20) (1997).
[8] Y. Yamada-Takamura, Z.T. Wang, Y. Fujikawa, T. Sakurai, Q.K. Xue, J. Tolle, P.L. Liu, A.V.G. Chizmeshya, J. Kouvetakis, I.S.T. Tsong, Phys. Rev. Lett. 95 (26) (2005) 266105.
[9] T. Oder, P. Martin, J. Lin, H. Jiang, J. Williams, T. Isaacs-Smith, Appl. Phys. Lett. 88 (18) (2006) 183505.
[10] J.M. Ziman, Electrons and phonons: the Theory of Transport Phenomena in Solids, Oxford University Press, 1960.
[11] G. Mahan, M. Bartkowiak, Appl. Phys. Lett. 74 (7) (1999) 953–954.
[12] M.J. Thompson, W.G. Fahrenholtz, G.E. Hilmas, J. Am. Ceram. Soc. 95 (3) (2012) 1077.
[13] J.W. Zimmermann, G.E. Hilmas, W.G. Fahrenholtz, R.B. Dinwiddie, W.D. Porter, H. Wang, J. Am. Ceram. Soc. 91 (5) (2008) 1405.
[14] L. Zhang, D.A. Pejaković, J. Marschall, M. Gasch, J. Am. Ceram. Soc. 94 (8) (2011) 2562.
[15] J.W. Lawson, M.S. Daw, C.W. Bauschlicher Jr, J. Appl. Phys. 110 (8) (2011) 083507.
[16] H. Kinoshita, S. Otani, S. Kamiyama, H. Amano, I. Akasaki, J. Suda, H. Matsunami, Jpn. J. Appl. Phys. 40 (12A) (2001) L1280.
[17] D.A. Broido, A. Ward, N. Mingo, Phys. Rev. B 72 (1) (2005) 014308.
[18] W. Li, N. Mingo, Phys. Rev. B 89 (18) (2014) 184304.
[19] J.-.Y. Yang, G. Qin, M. Hu, Appl. Phys. Lett. 109 (24) (2016) 242103.
[20] L. Lindsay, D.A. Broido, T.L. Reinecke, Phys. Rev. B 87 (16) (2013) 165201.

[21] W. Zhang, J.-.Y. Yang, L. Liu, RSC Adv. 9 (3) (2019) 1387–1393.
[22] C. Li, N.K. Ravichandran, L. Lindsay, D. Broido, Phys. Rev. Lett. 121 (17) (2018) 175901.
[23] A.J. McGaughey, A. Jain, Appl. Phys. Lett. 100 (6) (2012) 061911.
[24] J. Noffsinger, F. Giustino, B.D. Malone, C.-.H. Park, S.G. Louie, M.L. Cohen, Comput. Phys. Commun. 181 (12) (2010) 2140.
[25] F.G.J. Noffsinger, B.D. Malone, C.-.H. Park, S.G. Louie, and M.L. Cohen, arXiv preprint arXiv:1604.03525 (2016).
[26] X. Liang, Phys. Rev. B 95 (15) (2017) 155313.
[27] P. Giannozzi, S. Baroni, N. Bonini, M. Calandra, R. Car, C. Cavazzoni, D. Ceresoli, G.L. Chiarotti, M. Cococcioni, I. Dabo, et al., J. Phys. Conden. Matter 21 (2009) 395502.
[28] M. Schlipf, F. Gygi, Comput. Phys. Commun. 196 (2015) 36–44.
[29] W. Li, J. Carrete, N.A. Katcho, N. Mingo, Comput. Phys. Commun. 185 (6) (2014) 1747–1758.
[30] L. Lindsay, D. Broido, T. Reinecke, Phys. Rev. Lett. 111 (2) (2013) 025901.
[31] Y.G. Naidyuk, O.E. Kvitnitskaya, I.K. Yanson, S.L. Drechsler, G. Behr, S. Otani, Phys. Rev. B 66 (14) (2002) 140301.
[32] S. Sichkar, V. Antonov, V. Antropov, Phys. Rev. B 87 (6) (2013) 064305.
[33] R. Heid, B. Renker, H. Schober, P. Adelmann, D. Ernst, K.P. Bohnen, Phys. Rev. B 67 (18) (2003) 180510.
[34] J. Noffsinger, F. Giustino, S.G. Louie, M.L. Cohen, Phys. Rev. B 77 (18) (2008) 180507.
[35] W. Weber, Phys. Rev. B 8 (11) (1973) 5082.
[36] A.N. Christensen, W. Kress, M. Miura, N. Lehner, Phys. Rev. B 28 (2) (1983) 977.
[37] T. Tanaka, Y. Ishizawa, E. Bannai, S. Kawai, Solid State Commun. 26 (12) (1978) 879–882.
[38] Q. Zheng, A.B. Mei, M. Tuteja, D.G. Sangiovanni, L. Hultman, I. Petrov, J.E. Greene, D.G. Cahill, Phys. Rev. Mater. 1 (6) (2017) 065002.
[39] A. Kokalj, J. Mol, Graphics Modell. 17 (3) (1999) 176–179.